Control of Starter Generator in a UAV with a Micro Jet Engine

Jun-ichi Itoh[*a]   Senior Member,   Kazuki Kawamura[*]   Member
Keisuke Kusaka[*]   Member,   Yoshiya Ohnuma[**]   Member
Hiroyuki Koshikizawa[***]   Non-member,   Kazuyuki Abe[***]   Non-member

A control method of a starter generator, which are for a jet engine for an unmanned aerial vehicle (UAV) system is proposed in this paper. Both the jet engine and the propellers that are powered by the jet engine via a starter generator generates the thrust power. Using the jet engine for obtaining the thrust, it is possible to extend a flight range since the energy density of the jet engine of the developed system is higher than the energy density of the battery in the conventional system. The miniaturization is also achieved by connecting the starter generator to the jet engine because high-frequency operation makes the starter generator compact. The proposed control strategy achieves the starting, powering, and cooling operations using the starter generator. Each operation is demonstrated with a 3-kW prototype. As the results, the maximum conversion efficiency of 92.7% is observed. Moreover, the minimum total harmonic distortion of the generator current is 16.5% at the rated operation speed (70000 r/min). Further, the exhaust nozzle temperature is stabilized within the maximum deviation of 2% of the command in a steady state.

Keywords: starter generator, jet engine, unmanned aerial vehicle (UAV), V/f control

1. Introduction

In recent years, UAVs have been actively studied for rescue activities in natural disasters [1]–[4]. Specifically, the multicopter-type UAV has two features: the multicopter UAV does not require a designated landing space, the unmanned operation makes it possible to approach danger zones. In UAVs, which had been previously developed, the multicopter UAV is generally powered by batteries [2]. Due to the limitation of the battery energy density [5], a loading weight and a flight range are limited. In order to overcome this disadvantage, a UAV with a jet engine has been developed [6]. Thrust is generated via both the jet engine and propellers that are powered by the jet engine through the starter generator in the developed UAV system. Using the jet engine as a thrust generator, the flight range can be extended because the energy density of the jet engine and fuel is greater than the energy density of the battery. Furthermore, the jet engine with remaining fuel can be used as an emergency power supply using the starter generator after the flight.

An auxiliary power unit (APU) is generally used for starting and cooling the jet engine [7][8]. The use of APU has the problem, which causes the increases in the cost and size of the system because the rotation speed of the generator, which is connected via reduction gears [9][10] to the jet engine, in APU is low. Due to the low speed, a volume of the generator tends to be large in a high-power UAV system.

A UAV system with a jet engine and its control strategy of the starter generator are proposed in this paper. In the system, only the starter generator have the role of starting and cooling operation without an APU. Furthermore, the starter generator is directly connected to the jet engine without a reduction gear and rotated at high speed for miniaturization. The challenge in the study is achieving the stable operation and mode shift among the operation modes; starting mode, powering mode, and cooling mode, by the proposed control scheme. In particular, the synchronous frequency command limiter and output power limiter is implemented for the stable operation in the proposed control method. Additionally, new modulation method using a modified carrier via the estimated intersection phase based on synchronous PWM is experimentally demonstrated. The experimental results show that the prototype achieves a maximum conversion efficiency of 92.7%, and the minimum THD of the generator current is 16.5% at a rotation speed of 70000 r/min. Additionally, a temperature of an exhaust nozzle is controlled within the maximum deviation of 2% in comparison with the command temperature in the steady state.

2. System Configuration of UAV System

Figure 1 shows the configuration of the UAV system, which is developed in this paper. The feature of this system is that it has no reduction gears between the jet engine and the starter generator. The jet engine supplies power to six propellers through the starter generator. For the aerial applications, weight reduction of the starter generator is important issue from the view of extending a flight range. Thus, the high rotation speed is required for miniaturization and weight

a) Correspondence to: Jun-ichi Itoh. E-mail: itoh@vos.nagaoka ut.ac.jp
* Nagaoka University of Technology
  1603-1, Kamitomioka, Nagaoka, Niigata 940-2188, Japan
** Nagaoka Power Electronics Co., Ltd.
  2085-16, Fukasawa, Nagaoka, Niigata 940-2135, Japan
*** YSEC Co., Ltd.
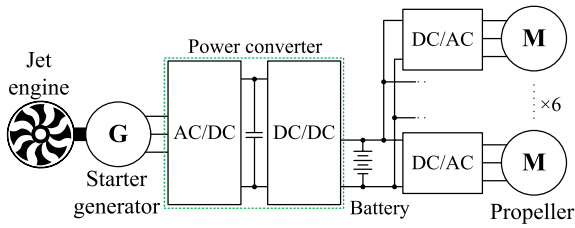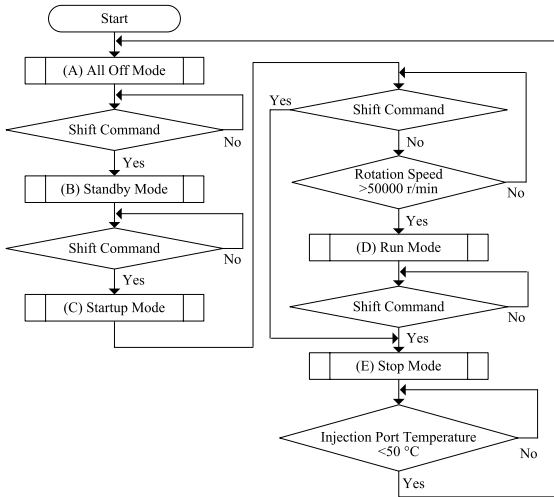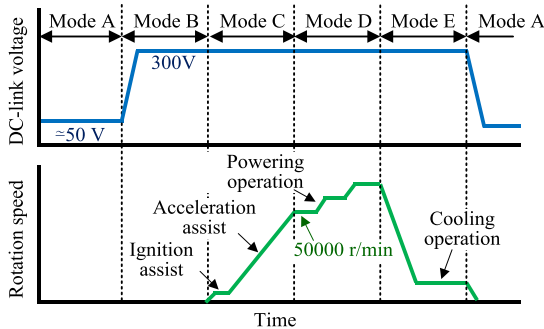 8460-1, Urushiyama, Nishi-kanku, Niigata 953-0054, Japan

Fig. 1. System configuration of the developed UAV system

(a) Flowchart of the mode change of the proposed UAV system.

(b) Mode transition of the jet generator.

Fig. 2. Diagram of the mode transition for the developed UAV system

reduction.

Figure 2 is the diagram of the mode transition of the UAV system. An operation mode is selected by a host controller. There are five operation modes as shown below.

A. All off Mode

The mode is a stationary state. The power converters are not activated. It means that all of the switches are off.

B. Standby Mode

The DC-DC converter is activated. The DC-DC converter boosts the DC-link voltage from the battery voltage to 300 V. In this mode, the AC/DC converter is not activated.

C. Startup Mode

The AC/DC converter is activated. The starter generator assist in both the ignition of the jet engine and acceleration up to 50000 r/min. The host controller controls the starter generator speed in the aforementioned state. The temperature of the exhaust nozzle of the jet engine is also controlled.

D. Run Mode

The system is operated with the powering operation within the rotation speed range from 50000 to 70000 r/min, and the battery is charged. The jet engine controls the speed while the starter generator controls the output power.

E. Stop Mode

The engine output is halted then the starter generator decelerates and cools the jet engine. The operation of the power converter continues till the temperature of the exhaust nozzle of the jet engine cool down to 50°C or lower. Subsequently, the operation mode is shifted to the all-off mode.

3. Modulation for Suppressing Even-order Harmonic Components

3.1 Continuous PWM The generator current composes the low-order harmonic components and beat components because the carrier frequency and the fundamental frequency are closed owing to the direct connection of the generator and the jet engine. For the high-frequency operation, the nine-pulse synchronous PWM technique is implemented during the Run Mode.

Figure 3 shows the voltage command of the continuous PWM. In this figure, the waveforms with a modulation index of 0.8 and a triangular carrier with a frequency ratio of nine are illustrated. As shown in Fig. 3(a), PWM signal is generally generated by comparing the voltage command v_u^* and the triangular carrier. Figure 3(b) shows the modulation index command V_m^* and modified carrier u_{mc}. The modified carrier is used for the carrier comparison. The modified carrier u_{mc} is expressed by

$$u_{mc} = \frac{u_m}{\sin \theta} \quad (\theta \neq 0 \deg, \ 180 \deg) \cdots\cdots\cdots\cdots\cdots (1)$$

where θ denotes the phase of voltage command and u_m denotes the triangular carrier.

The intersection phase of the modulation signal and the carrier is estimated by using a look-up table of the modified carriers in a DSP in the proposed modulation method. Then a voltage command based on the estimated intersection phase is output. The proposed control can be implemented to a micro-controller because the proposed modulation method does not need a change of the hardware.

Table 1 shows the estimated intersection phase patterns of the continuous PWM. Due to the synchronous PWM, the estimated intersection phases of sectors zero and nine are determined as 0° and 180°, respectively as shown in Table 1. The relationship between the phase and modulation index command of the modified carrier u_{mc} of sectors 1, 2, 3, and 4 is
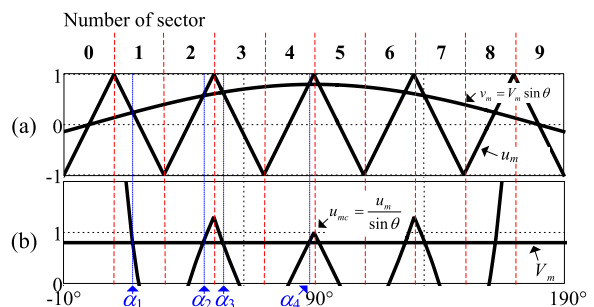

Fig. 3. Waveforms of the voltage commands and carriers with the continuous PWM

Table 1. Estimation of phase patterns with the continuous PWM

Sector	Look Up Table	Phase of Intersection Point	Sector	Look Up Table	Phase of Intersection Point
0	/	0°	9	/	180°
1	1	α_1	10	1	180°+α_1
2	2	α_2	11	2	180°+α_2
3	3	α_3	12	3	180°+α_3
4	4	α_4	13	4	180°+α_4
5	4	180°-α_4	14	4	360°-α_4
6	3	180°-α_3	15	3	360°-α_3
7	2	180°-α_2	16	2	360°-α_2
8	1	180°-α_1	17	1	360°-α_1

α_X : Phase by Look Up Table X

Table 2. Estimation of phase patterns with the discontinuous PWM

Sector	Look Up Table	Phase of Intersection Point	Sector	Look Up Table	Phase of Intersection Point
0	/	0°	9	/	180°
1	1	α_1	10	1	180°+α_1
2	2	α_2	11	2	180°+α_2
3	3	α_3	12	3	180°+α_3
4	/	90°	13	/	270°
5	/	90°	14	/	270°
6	3	180°-α_3	15	3	360°-α_3
7	2	180°-α_2	16	2	360°-α_2
8	1	180°-α_1	17	1	360°-α_1

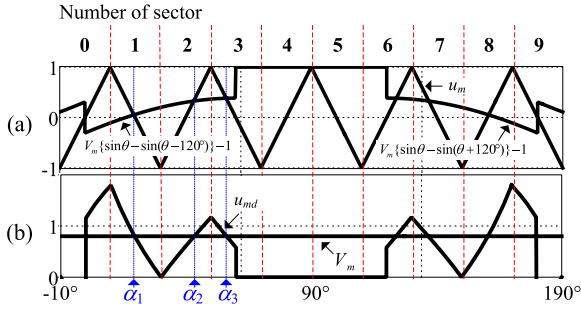α_X : Phase by Look Up Table X

Fig. 4. Waveforms of the voltage commands and carriers with the discontinuous PWM

shown in Tables 1, 2, 3, and 4. It should be noted that α_1, α_2, α_3, and α_4 correspond to the estimated intersection phases referred to the look-up tables. With respect to sector five and above, it is not necessary to prepare the tables to estimate the phase by using the symmetry at every 90 deg. The proposed modulation method obtains the estimated intersection phase in each sector using the phase according to look-up tables 1 to 4 and the relationship in Table 1 and outputs a voltage command based on the estimated intersection phase. The generated PWM signal is equivalent to that generated via the analog control. Therefore, even-order harmonic components are not composed on the generator current.

3.2 Discontinuous PWM　　Figure 4 shows the carrier comparison of discontinuous PWM when a frequency ratio of the carrier signal to the modulation signal is nine. The waveforms with a modulation index of 0.8 is illustrated in thig figure. The discontinuous PWM signal $v_{xd}{}^*$ shown in Fig. 4(a) is calculated by adding the following offset to the three-phase modulation signal v_x:

$$v_{xd}^* = v_x^* + v_{offset}^*, \ (x = u, v, w)$$

$$v_{offset}^* = \begin{cases} 1 - |v_{\max}| & \text{if } |v_{\max}| \geq |v_{\min}|, \\ -1 + |v_{\min}| & \text{if } |v_{\min}| < |v_{\max}|, \end{cases} \ \cdots\cdots (2)$$

$$\text{and} \begin{cases} v_{\max} = \max[v_u^*, v_v^*, v_w^*] \\ v_{\min} = \min[v_u^*, v_v^*, v_w^*] \end{cases}$$

A modified carrier u_{md} shown in Fig. 4(b) is used as mentioned in Section A. The intersection phases in sectors zero and four are defined as 0 deg. and 90 deg., respectively, in advance. Therefore, the modified carriers of sectors one, two, and three are only required to estimate the intersection phases. The modified carrier u_{md} is calculated by (2) in the discontinuous PWM.

$$u_{md} = \frac{u_m + 1}{\sin \theta - \sin(\theta - 120°)} \quad (10° \leq \theta < 60°) \cdots (3)$$

It should be noted that in the section exceeding 60 deg. in sector three, the intersection phase is set to 60 deg. when the modulation index is 0.577 or lower.

Table 2 lists the estimated intersection phase patterns of the discontinuous PWM. The relationship between the phase and modulation index command of the deformed carrier u_{md} of sectors one, two, and three is defined as given in look-up Tables 1, 2, and 3. By referring the phases α_1, α_2, and α_3 via the modulation index from the look-up tables, the intersection phase of the carrier and modulation signal in each sector is estimated by the relationship shown in Table 2. By using the method, the symmetry of the PWM signal is ensured even in the discontinuous modulation, and the even-order harmonic components is not appear on the generator current.

4. Control Scheme for Starter Generator

Figure 5 shows the configuration of the power converters. The system has an interleaved DC-DC converter with four legs and a three-phase inverter. The DC-DC converter is used because the battery voltage is approximately 50 V. The DC voltage must be boosted to 300 V for the drive of the inverter.

Figure 6 shows the control block diagram of the DC-DC converter. The DC-DC converter regulates the DC link voltage V_{dc} to the voltage command. The current is independently controlled in each leg to suppress the current
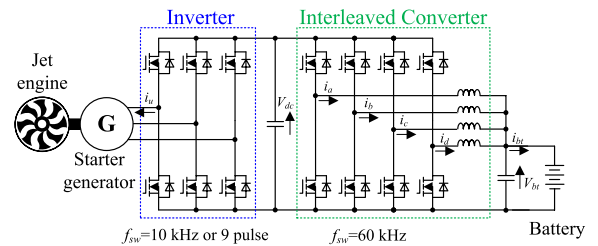

Fig. 5. System configuration of the starter generator and interleaved DC-DC converter
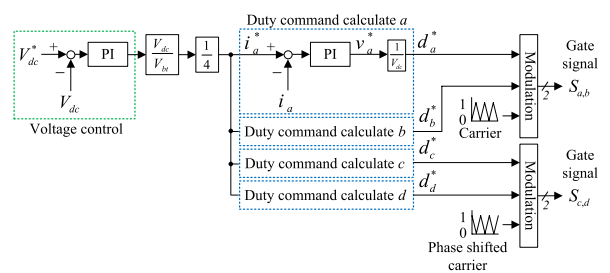

Fig. 6. Block diagram of the interleaved DC-DC converter
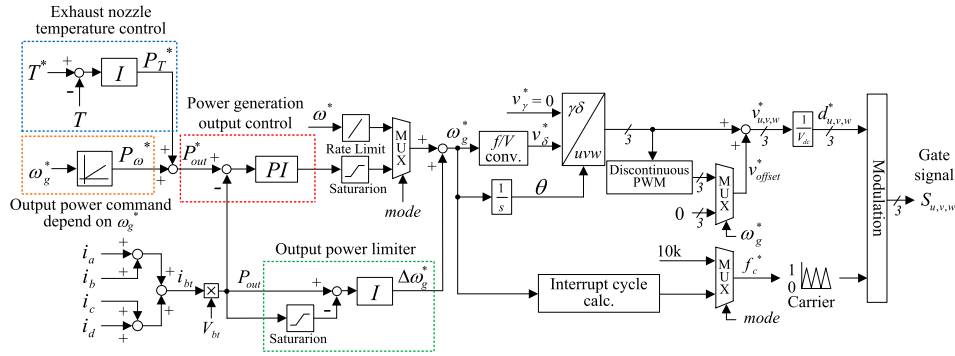
Fig. 7. Control block diagram of the 3-phase inverter

imbalance among four legs. The carrier for two legs is phase-shifted by half the switching period. Thus, the current ripple is reduced to half [11] of the non-interleaved DC/DC converter because the switching frequency is equivalently doubled.

Figure 7 shows the control block diagram of the AC-DC converter. The V/f control is employed except the run mode. In the run mode, a power control is necessary for stable operation of the jet engine.

The rotation speed of the jet engine may suddenly decrease at the mode change from the V/f control to the output power control or exhaust nozzle temperature control when the output power of the jet engine is not sufficiently high. Hence, the stable operation of the jet engine at a low speed is difficult. In order to overcome the problem, a synchronous frequency command limiter is applied. By the frequency command limit, the speed is maintained at constant until the jet engine output becomes sufficiently high. Besides, the generator torque may suddenly changes during the startup mode. In order to prevent the converter from the overcurrent during the operation, an output power limiter is implemented. The synchronous frequency command is compensated to avoid the sudden change in the torque. Around the rated speed, discontinuous PWM is employed to achieve the operation in an over-modulation region.

5. Stabilization Analysis of the Power Generation Output Control

Figure 8 shows the relation between the rotation speed and the thrust of the jet engine. A thrust of 68.0 N is obtained at the rotation speed of 70000 r/min. Assuming that the atmospheric temperature and air density are constant under the atmospheric pressure, the thrust of the jet engine depends on only the rotational speed irrespective of the output power. The thrust of the jet engine is proportional to the cube of the rotational speed, and thus, the thrust F obtained by the measured value is approximated by the cube of the rotational speed as follows:

$$F = k_F \omega^3 \cdots\cdots\cdots\cdots\cdots\cdots\cdots\cdots\cdots\cdots\cdots\cdots (4)$$

where k_F denotes the coefficient obtained from the experiment, and ω denotes the rotation speed of the jet engine.

Figure 9 shows the block diagram of the output power control system with the jet engine. In the proposed system, synchronous angular frequency ω_g of the generator is generated via the difference between the output power command P_{out}^* and detected output power P_{out}. In addition, it is assumed that
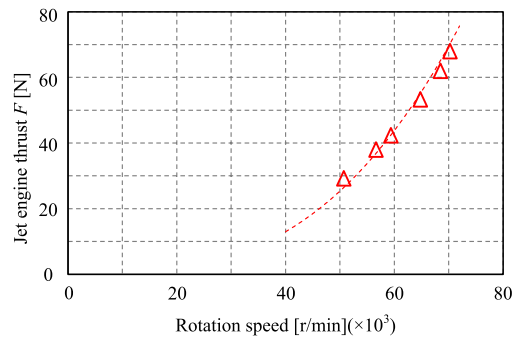

Fig. 8. Relation between the rotation speed and thrust of the jet engine
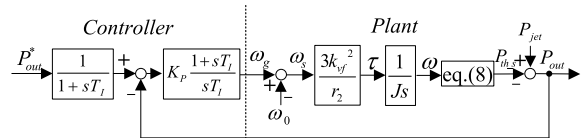

Fig. 9. Control block diagram of the output power with the jet engine

the response of the rotation speed control for the jet engine is sufficiently slower than the response of the output power control. Assuming that the loss can be ignored, the total power of the jet engine P_{jet} is calculated as follows:

$$P_{jet} = P_{th} + P_{out} \cdots\cdots\cdots\cdots\cdots\cdots\cdots\cdots\cdots\cdots\cdots (5)$$

where P_{th} is the thrust power of the jet engine. The thrust power is added to the shaft power P_{out} that drives the propeller. The shaft power is determined by the flight speed and thrust of the aircraft. However, if the aircraft is stationary as in the test, the shaft power cannot be calculated from the flight speed. In this case, the stationary shaft power P_{th_s} is calculated as follows:

$$P_{th\_s} = \frac{F}{11.2} \times 736 \cdots\cdots\cdots\cdots\cdots\cdots\cdots\cdots\cdots\cdots (6)$$

Substituting (4) into (6), the stationary shaft power [12] is calculated as follows

$$P_{th\_s} = \frac{736 k_F}{11.2} \omega^3 = k_{th} \omega^3 \cdots\cdots\cdots\cdots\cdots\cdots\cdots (7)$$

with the coefficient k_{th}:

The rotation angular velocity is linearized to analyze the stability of the control around the steady state by (8).

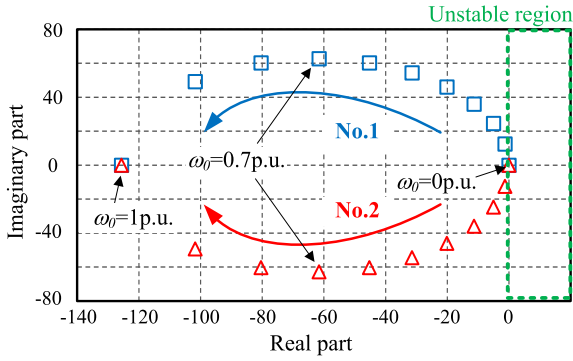$$P_{th\_s} = 3 k_{th} \omega_0^2 \omega \cdots\cdots\cdots\cdots\cdots\cdots\cdots\cdots\cdots\cdots\cdots (8)$$

Fig. 10. Roots locus with changing the initial angular velocity ω_0

Fig. 11. Step response of output power with the change of output power command from 0.3 p.u. to 0.5 p.u

It should be noted that ω_o denotes the initial angular velocity at the steady-state point. Thus, the transfer function from input to output of the control system is expressed as follows:

$$G(s) = \frac{-\dfrac{9K_p k_{vf}{}^2 k_{th} \omega_0{}^2}{K_i r_2 J}}{s^2 - \dfrac{9K_p k_{vf}{}^2 k_{th} \omega_0{}^2 s}{r_2 J} - \dfrac{9K_p k_{vf}{}^2 k_{th} \omega_0{}^2}{K_i r_2 J}}$$

$$\cdots\cdots\cdots\cdots\cdots\cdots (9)$$

where r_2 denotes the secondary winding resistance of the generator, J is the total inertia of the jet engine and generator, k_{vf} is the voltage coefficient in the v/f control, K_p is the proportional control gain, and K_i is the integral control gain. Furthermore, the gain K_i and K_p are expressed as functions of the response angular frequency ω_n and damping coefficient ζ.

$$K_p = -\frac{2\xi \omega_n r_2 J}{9 k_{vf}{}^2 k_{th} \omega_0'^2} \cdots\cdots\cdots\cdots\cdots\cdots\cdots (10)$$

$$K_i = \frac{2\xi}{\omega_n} \cdots\cdots\cdots\cdots\cdots\cdots\cdots\cdots\cdots (11)$$

It should be noted that ω_0' is the initial speed. The angular speed should be set accordingly to the detection value of the angular speed. However, the angular velocity detection is not employed in the test, and thus, the value is predetermined as follows.

Figure 10 shows the roots locus with changing the initial angular velocity ω_0. In the system, the powering operation is performed in the rotation speed range from 0.7 to 1.0 p.u. Therefore, the initial angular velocity setting value ω_0' is 0.7 p.u. The damping coefficient ζ is designed to be 0.7. The response angular frequency ω_n is designed for making overshoot time 0.05 s; this is 1/10 of the control period of the jet engine. As shown in Fig. 10, the control system is on the instability threshold when the rotation speed is 0 p.u. because the poles are located on the imaginary axis. The control system is always stable because the poles move to the negative half plane when the rotation speed exceeds 0 p.u.

Figure 11 shows the step response of output power when the output power command changes from 0.3 p.u. to 0.5 p.u. As shown in Fig. 11, the response equals or exceeds the design response time at rotation speeds of 0.7 p.u. and 1.0 p.u. The response time is delayed, and a large overshoot occurs in output power at the rotation speeds of 0.4 p.u. and 0.1 p.u.,
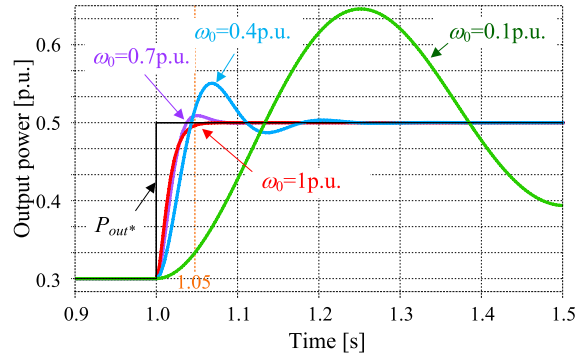
and this corresponds to the low-speed range. However, this type of large overshoot does not occur because the power generation operation is only performed in the high-speed range in the system.

6. Experimental Results

6.1 Modulation Method for Even-order Harmonic Component Suppression Figure 12 shows the experimental system. Table 3 shows the specification of the starter generator. In this test, the induction motor is mechanically connected to the generator to emulate the jet engine. Additionally, a small-capacity DC power supply is connected to the DC-ling via the diode. The DC power supply is used to supply the excitation current at the time of starting instead of the battery because the starter generator is an induction generator.

Figure 13 shows a block diagram of the three-phase PWM converter. The control system adjusts the slip angle frequency and controls the DC-link voltage. In the high-speed range, the modulation scheme is shifted from the asynchronous PWM to the synchronous PWM. The discontinuous PWM is selected around the rated speed to keep the operation even in the over-modulation region.
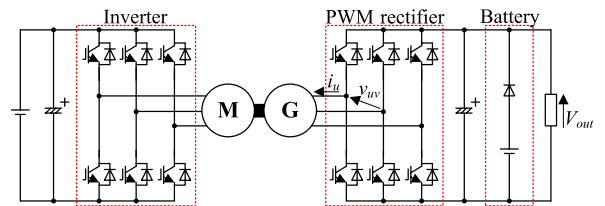

Fig. 12. Experimental setup

Table 3. Specifications of the starter generator

Parameter	Value
Poles	2
Rated rotary field speed	70000 r/min
Rated speed	68271 r/min
Rated voltage	200 V
Rated current	15.3 A
Rated power	4 kW
Rated torque	0.6 N·m
Weight	3.0 kg
Diagram	110 mm
Full length	192 mm

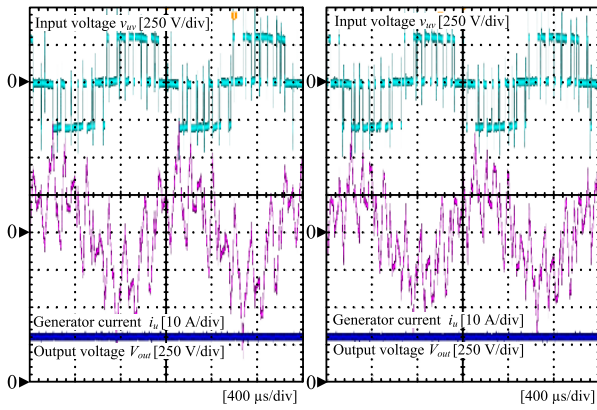Fig. 13. Control block diagram of the three-phase PWM converter

(a) Conventional method.　　　(b) Proposed method.
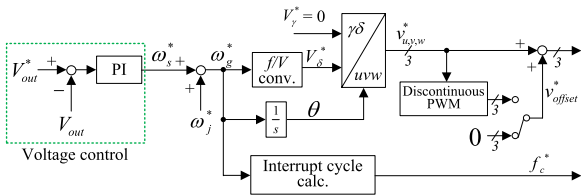
Fig. 14. Operation waveforms of PWM converter with the continuous PWM

(a) Conventional method.

(b) Proposed method.
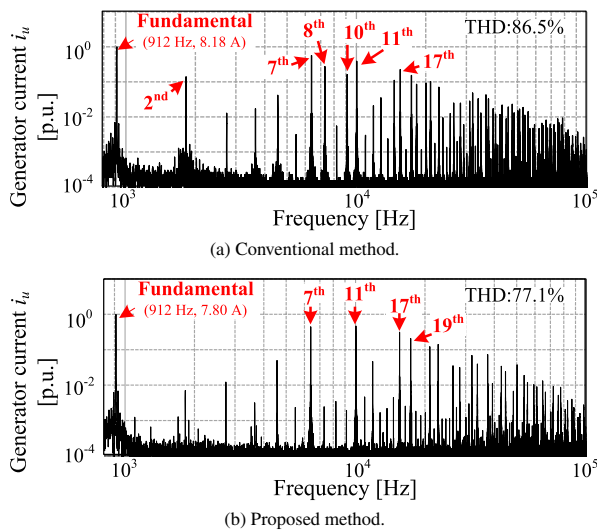
Fig. 15. Harmonics analysis of the generator current with the continuous PWM

(a) Conventional method.　　　(b) Proposed method.

Fig. 16. Operation waveforms of PWM converter with the discontinuous PWM

(a) Conventional method.

(b) Proposed method.

Fig. 17. Harmonics analysis of the generator current with the discontinuous PWM

Figure 14 shows the operation waveforms of the AC/DC converter with continuous PWM. The frequency ratio of the carrier frequency and the output frequency is nine and the rotation speed of 0.8 p.u. The waveforms are the input voltage of AC-DC converter, generator current, and output DC voltage. The modulation index is 0.871, and the conventional and proposed methods control the output voltage at constant (300 V).

Figure 15 shows the harmonic analysis of the generator current of the continuous PWM. As shown in Fig. 15(b), the proposed method is effective to suppress low even-order harmonic components, such as the second, eighth, and tenth order components, which are generated by the conventional method. In addition, the eighth harmonic component
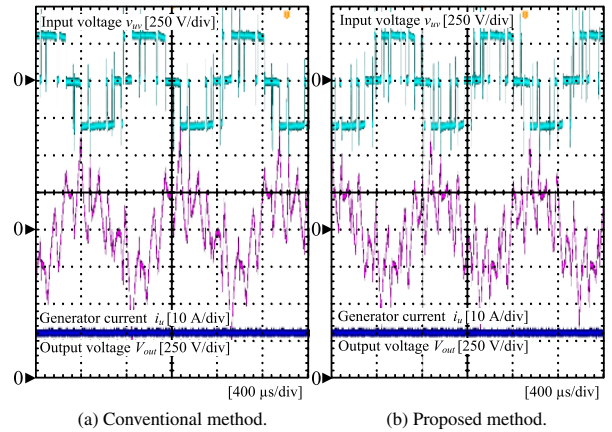
is reduced by 99.2% in comparison with the conventional method. Besides, total harmonic distortion (THD) of the generator current is reduced by 9.99% compared to that in the conventional method.

Figure 16 shows the operation waveforms of the discontinuous PWM at a rotation speed of 1.0 p.u. The frequency ratio of the carrier frequency to the output frequency is nine. The modulation index is 1.08, and the conventional method and proposed method control the output voltage at a constant value at 300 V.

Figure 17 shows the result of a harmonic analysis of the generator current with the discontinuous PWM. As shown in Fig. 17(b), the proposed method is effective to suppress low even-order harmonic components, such as the second, eighth, and tenth order components, which are generated by the conventional method. Additionally, the eighth harmonic component is reduced by 99.1% in comparison with that in the conventional method. Beside, THD of the generator current is reduced by 7.14% compared to that in the conventional method.

From the above experiments, the effectiveness of the proposed modulation methods in both the discontinuous PWM and the continuous PWM are verified.

6.2　Control Strategy for Starter Generator　　Table 4

Table 4. Specification of the jet engine

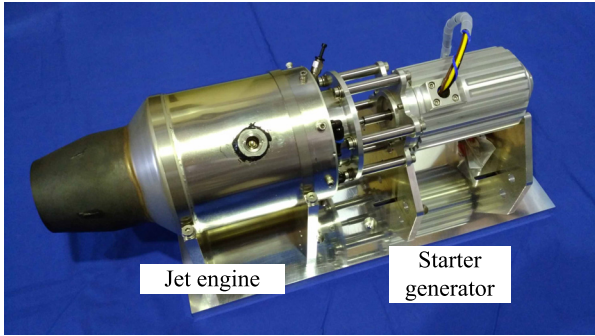| Parameter	Value
Weight	2.9 kg
Diameter	131 mm
Full length	281 mm
Rated thrust	165 N
Rated speed	100000 r/min

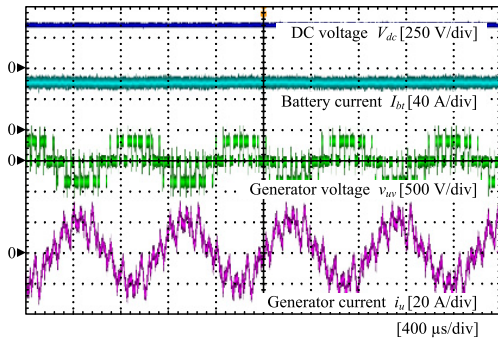Fig. 18. Developed jet engine and generator

Fig. 19. Operation waveforms when the generator is operated in the Run Mode
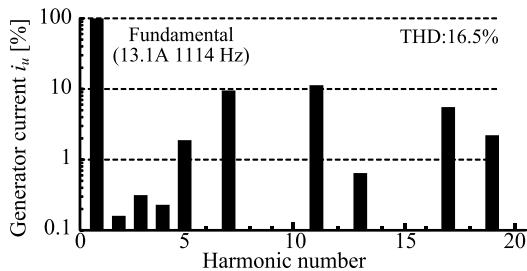

Fig. 20. Harmonic components on the generator current during the Run mode shown in Fig. 19

and Figure 18 and shows the specifications of the jet engine and the prototype of the jet generator, respectively. The starter generator and the jet engine are mechanically connected without a reduction gear.

Figure 19 shows the experimental waveforms of the AC-DC converter during the Run Mode. The rotation speed is a rated speed of 70000 r/min. The output power is 2.98 kW. The DC link voltage is regulated at 300 V. Moreover, a stable power generation operation is achieved because the battery current is constant at any rotation speed.

Figure 20 shows the harmonic components on the generator current, which is shown in Fig. 19. As shown in Fig. 20,
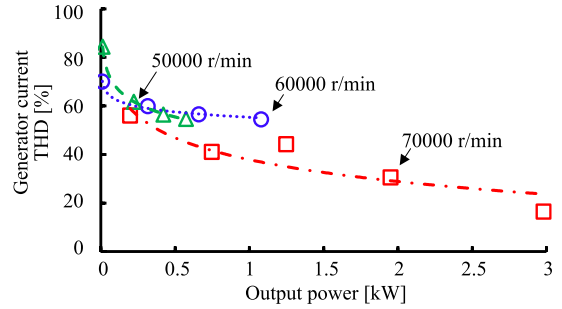

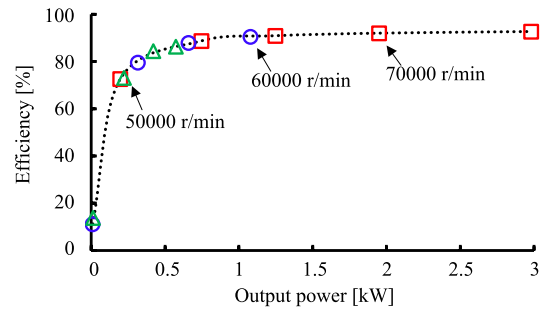Fig. 21. THD characteristics of the generator current

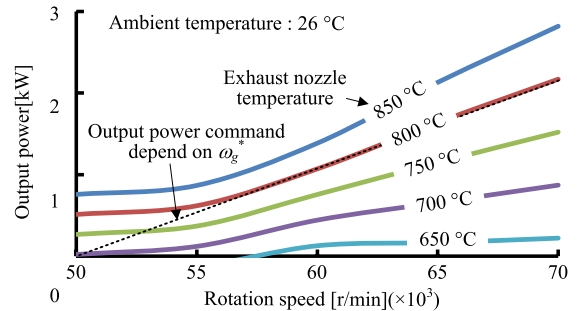Fig. 22. Efficiency characteristics of the power converter

Fig. 23. Characteristics of the exhaust nozzle temperature relative to rotation speed and output power and output power command based on rotation speed

even-order low harmonic components are less than 0.2%, and this is sufficiently smaller than the fundamental component.

Figure 21 shows the characteristics of the generator current THD relative to output power. As shown in Fig. 21, a minimum current THD of 16.5% is achieved with an output power of 2.98 kW at the rotation speed of 70000 r/min. This is because the fundamental component of the generator current increases when the output power increases.

Figure 22 shows the efficiency characteristics of the proposed system. Figure 22 shows that a maximum efficiency of 92.7% is achieved with an output power of 2.98 kW at a rotation speed of 70000 r/min.

Figure 23 shows the temperature characteristics of the exhaust nozzle relative to rotation speed, and the output power when the ambient temperature is 26°C. The output power increases with increasing in the rotation speed of the jet engine at the same exhaust nozzle temperature. Additionally, the system exhibits highest efficiency when the exhaust nozzle temperature is approximately 800°C. Therefore, an output power command depending to the rotation speed should
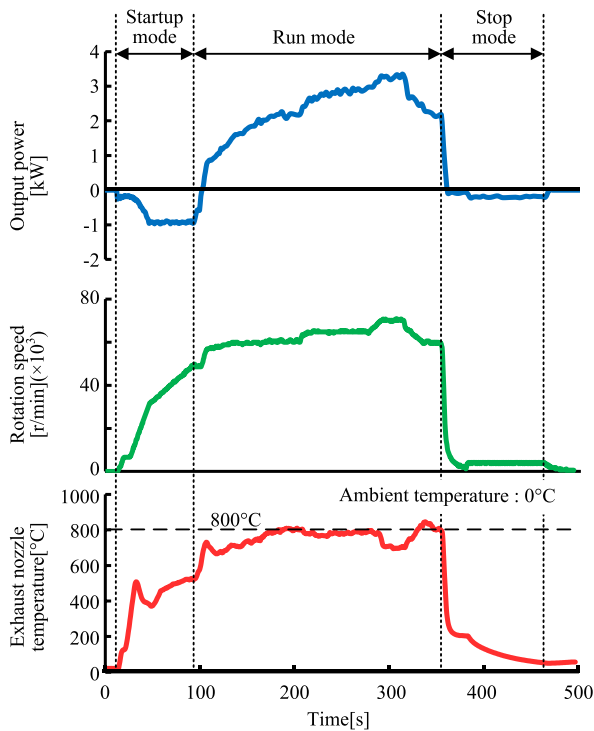
Fig. 24. Experimental results of operation of jet generator

be determined on the dotted line in Fig. 23.

Figure 24 shows the experimental results of the jet generator operation with the exhaust nozzle temperature control. The exhaust nozzle temperature command is 800°C. The jet engine is accelerated to 60000 r/min, 65000 r/min, and 70000 r/min in the run mode. Subsequently, the jet engine is decelerated to 60000 r/min. As shown in Fig. 24, even when the rotation speed accelerates or decelerates, the exhaust nozzle temperature converges to the command value. The exhaust nozzle temperature can be controlled within the maximum deviation of 2% of the command value in the steady state. Around the 300 s, the exhaust nozzle temperature at 70000 r/min decreases from 800°C to 700°C because the inflow current of the battery is limited for the protection. From this result, the proposed control method achieves the starting, powering, and cooling operations. Transition without the deceleration is achieved via the synchronous frequency command limiter when the startup mode changes to the run mode.

The output power gradually approaches zero after the transition because the starter generator maintains the rotation speed until the output power of the jet engine becomes sufficiently high. The acceleration without overload is achieved in the startup mode via an output power limiter, and this limits a command to 1 kW. Furthermore, the starter generator decelerates by a free run when the operation mode transitions to the stop mode from the run mode. Subsequently, the inverter restarts at a rotation speed of 1000 r/min. The starter generator simultaneously performs the cooling operation.

7. Conclusion

In the study, the control method of the starter generator for a UAV with a jet engine has been proposed. Stable transition

without decelerating and overcurrent among the operation modes is achieved using the synchronous frequency command limiter and the output power limiter. Additionally, the suppression method of the low even-order harmonic components, which is caused when the output frequency and the carrier frequency is closed, are demonstrated. The proposed modulation method uses the estimated intersection phase for the synchronous PWM. The 3-kW prototype system achieves minimum generator current THD of 16.5% at a rated rotational speed of 70000 r/min. At the rotational speed, a maximum conversion efficiency of the prototype is 92.7%. Additionally, the exhaust nozzle temperature is controlled within the maximum deviation corresponding to 2% of the command value.

References

(1) C. Satici, H. Poonawala, and M.W. Sppong: "Robust Optical Control of Quadrotor UAVs", IEEE Access, Vol.1, pp.79–93 (2013)

(2) N. Gageik, P. Benz, and S. Montenegro: "Obstacle Detection and Collision Avoidance for a UAV With Complementary Low-Cost Sensors", IEEE Access, Vol.3, pp.599–609 (2015)

(3) J. Shiau, D. Ma, P. Yang, G. Wang, and J. Gong: "Design of a Solar Power Management System for an Experimental UAV", IEEE Transactions on Aerospace and Electronic Systems, Vol.45, No.4, pp.1350–1360 (2009)

(4) J. Shiau, D. Ma, P. Yang, G. Wang, and J. Gong: "Predictor-Based Control of a Class of Time-Delay Systems and Its Application to Quadrotors", IEEE Transactions on Industrial Electronics, Vol.64, No.4, pp.459–469 (2016)

(5) M. Whittingham: "History, Evolution, and Future Status of Energy Storage", Proceedings of the IEEE, Vol.100, pp.1518–1534 (2012)

(6) "Small UAV turbojet engine developed in Japan", http://robohub.org/small-uav-tarbojet-engine-developed-in-japan/

(7) S. Chuangpishit, A. Tabesh, Z. Shahrbabak, and M. Saeedifard: "Topology Design for Collector Systems of Offshore Wind Farms With Pure DC Power Systems", IEEE Transactions on Industrial Electronics, Vol.61, No.1, pp.320–328 (2014)

(8) Y. Hirano, T. Yoshida, K. Ohishi, T. Miyazaki, Y. Yokokura, and M. Sato: "Vibration Suppression Control Method for Trochoidal Reduction Gears under Load Conditions", IEEJ J. Industry Applications, Vol.5, No.3, pp.267–275 (2016)

(9) T. Yoshioka, T.T. Phuong, A. Yabuki, K. Ohishi, T. Miyazaki, and Y. Yokokura: "High-performance Load Torque Compensation of Industrial Robot using Kalman-filter-based Instantaneous State Observer", IEEJ J. Industry Applications, Vol.5, No.3, pp.267–275 (2016)

(10) H. Kim, S.B. Lee, S. Park, S.H. Kia, and G.A. Capolino: "Reliable Detection of Rotor Faults Under the Influence of Low-Frequency Load Torque Oscillations for Applications With Speed Reduction Couplings", IEEE Transactions on Industry Applications, Vol.52, No.2, pp.1460–1468 (2016)

(11) T. Nakanishi and J. Itoh: "Control Strategy for Modular Multilevel Converter based on Single-phase Power Factor Correction Converter", IEEJ J. Industry Applications, Vol.6, No.1, pp.46–57 (2017)

(12) E. Torenbeek: "Synthesis of Subsonic Airplane Design", Kluwer Academic Publishers, pp.97–140 (2014)

Jun-ichi Itoh (Senior Member) was born in Tokyo, Japan, in 1972. He received his M.S. and Ph.D. degree in electrical and electronic systems engineering from Nagaoka University of Technology, Niigata, Japan in 1996, 2000, respectively. From 1996 to 2004, he was with Fuji Electric Corporate Research and Development Ltd., Tokyo, Japan. He was with Nagaoka University of Technology, Niigata, Japan as an associate professor. Since 2017, he has been a professor. His research interests are matrix converters, dc-dc converters, power factor correction techniques, energy storage system and adjustable speed drive systems. He received IEEJ Academic Promotion Award (IEEJ Technical Development Award) in 2007. In addition, he also received Isao Takahashi Power Electronics Award in IPEC-Sapporo 2010 from IEEJ, 58th OHM Technology Award from The Foundation for Electrical Science and Engineering, November, 2011, Intelligent Cosmos Award from Intelligent Cosmos Foundation for the Promotion of Science, May, 2012, and Third prize award from Energy Conversion Congress and Exposition-Asia, June, 2013. Prizes for Science and Technology (Development Category) from the Commendation for Science and Technology by the Minister of Education, Culture, Sports, Science and Technology, April 2017. Dr. Itoh is a senior member of the Institute of Electrical Engineers of Japan, the Society of Automotive Engineers of Japan and the IEEE.

Kazuki Kawamura (Member) was born in Japan, in 1993. He received his B.S. degree from National Institute of Technology, Niihama College, Japan in 2016. In 2018, he received his M.S. degree in electrical, electronics and information engineering from Nagaoka University of Technology, Niigata, Japan in 2018. Since 2018, he has been with Daikin Industries Ltd., Japan.

Keisuke Kusaka (Member) received his B.S. and M.S. degrees from Nagaoka University of Technology, Niigata, Japan in 2011, 2013, respectively. From 2015 to 2016, he was with Swiss Federal Institute of Technology in Lausanne (EPFL), Switzerland as a trainee. In 2016, he received his Ph.D. degree in energy and environment science from Nagaoka University of Technology. From 2016 to 2018, he was with Nagaoka University of Technology as a researcher. He is currently an assistant professor at Nagaoka University of Technology. His current research interests include an inductive power transfer system and high-frequency converters. He received the second prize paper award in IPEC-Niigata 2018.

Yoshiya Ohnuma (Member) received his M.S. and Ph.D. degrees in electrical, electronics and information engineering from Nagaoka University of Technology, Niigata, Japan in 2010 and 2013, respectively. Since 2013, he has been working at Nagaoka Power Electronics Co., Ltd. His research interests include power conversion system especially matrix converters, DC-DC converters and high-frequency techniques for power converters. He is a member of IEEE and IEEJ.

Hiroyuki Koshikizawa (Non-member) was born in Japan, in 1987. He received his B.S. degree in mechanical and control engineering from Niigata Institute of Technology, Niigata, Japan in 2008. Since 2010, he has been with YSEC Co., LTD. He has been worked on designing and developing a micro jet engine for UAV, medical equipment, and a food factory line.

Kazuyuki Abe (Non-member) was born in Japan, in 1971. He graduated Niigata prefectural maki high school in 1989. From 1989 to 2009, He was with KEISEI MEDICAL INDUSTRIAL Co., LTD. Since 2009, he has been with YSEC Co., LTD. He has been worked on designing and developing a micro jet engine for UAV, and medical equipment.